OPTICA

# Real-time waveguided quantum ghost imaging

Alexander Demuth,[1,*] Robin Camphausen,[1] Massimo Gandola,[2] Enrico Manuzzato,[2] Alessandro Tontini,[2] Leonardo Gasparini,[2] and Valerio Pruneri[1,3]

[1]ICFO-Institut de Ciencies Fotoniques, The Barcelona Institute of Science and Technology, 08860 Castelldefels, Barcelona, Spain
[2]Fondazione Bruno Kessler (FBK), 38123 Trento, Italy
[3]ICREA-Institució Catalana de Recerca i Estudis Avançats, Passeig Lluís Companys 23, 08010 Barcelona, Spain
*alexander.demuth@icfo.eu

Received 25 July 2025; revised 24 November 2025; accepted 25 November 2025; published 19 December 2025

**Imaging through waveguides such as optical fibers enables visualization of otherwise inaccessible regions, including deep biological tissue in endoscopy. Here, we demonstrate real-time waveguided quantum ghost imaging (wQGI) using a bright quantum light source and a single-photon avalanche diode image sensor. Our wide-field wQGI approach requires no active modulation and produces real-time coincidence images directly, due to the imager's on-chip, in-pixel correlation logic. Using a standard, commercial off-the-shelf fiber bundle compatible with standard endoscopic setups, we validate our system on test samples and quantitatively compare image quality to standard free-space QGI. QGI can enhance the signal-to-noise ratio in the low-photon regime. It also enables imaging at wavelengths where conventional image sensors lack sensitivity. The demonstrated platform thus provides a viable approach to non-invasive, low-light imaging in spectral regions not accessible by standard sensors.**



https://doi.org/10.1364/OPTICA.574234

## 1. INTRODUCTION

Optical imaging is perhaps the most important measurement technique in research and development, enabling diverse applications spanning from live-cell microscopy to industrial inspection. In recent years, quantum mechanics has been shown to enhance optical imaging and overcome classical limitations such as optical resolution or the signal-to-noise ratio (SNR) [1,2]. The field of quantum imaging has led to a range of ground-breaking advancements and novel modalities, such as quantum-enhanced Raman microscopy [3], super-resolution imaging [4,5], sub-shot noise and super-sensitive imaging [6,7], imaging with undetected photons [8], and quantum holography [9,10]. The earliest and one of the most striking examples of quantum imaging is quantum ghost imaging (QGI), where correlated photons allow the formation of an image from photons that have never interacted with the sample [11,12].

QGI typically employs spontaneous parametric down-conversion (SPDC) to generate photon pairs—"signal" and "idler"—with spatio-temporal correlations [13]. These pairs of photons are split into two beams: the idler illuminates the sample and is collected by a single-pixel ("bucket") detector that records only the time of arrival. Meanwhile, the signal is directly imaged with spatial resolution (e.g., by an image sensor), capturing both position and time of arrival. Correlating the measurements from both arms allows the extraction of an image based solely on the paired photons while discarding unpaired detections [14].

Since SPDC allows generating non-degenerate photon pairs, where the signal and idler have different frequencies, QGI enables imaging where the sample and the image sensor are illuminated with separate wavelengths [15,16]. This makes it possible to image at spectral ranges where suitable image sensor technology is not available, such as in the infrared [17–20]. In addition, QGI has been shown to offer improved SNR compared to classical schemes [21–23], enabling ultralow-light imaging [17]. These properties indicate the potential of QGI in biomedical and life sciences applications, where low illumination intensities help avoid photodamage to sensitive biological samples [24,25]. Moreover, QGI's ability to image in the infrared holds significant promise because infrared radiation often penetrates deeper into biological tissue and corresponds to an information-rich spectral region due to critical molecular transitions [26–28].

To date, QGI experiments have largely been restricted to direct free-space illumination. However, there is a need for imaging devices capable of observing regions of interest that are not directly accessible. In the biomedical field, for example, *in vivo* imaging of internal organs, or keyhole surgery, the object is often occluded from direct view by the presence of opaque biological tissue. Likewise, industrial inspection tasks frequently require imaging difficult-to-access areas such as the inside of turbines. Waveguide-based approaches such as flexible micro-endoscopes or borescopes, aim to fulfill this need. In classical imaging, such schemes initially employed single-mode, or few-core, fibers [29,30], often combined with scanning. Modern image fiber bundles contain tens of thousands of cores functioning as pixels, enabling high-quality visualization with minimal invasiveness [31–33]. Unlike multimode fiber endoscopes that require transfer-matrix calibration and

frequent realignment, imaging bundles provide a passive, stable one-to-one mapping of spatial modes. Extending QGI to such a waveguided system requires preservation of spatio-temporal correlations during transmission, which has recently been demonstrated [34,35].

In this work, we demonstrate real-time waveguided quantum ghost imaging (wQGI), thereby extending the unique capabilities of QGI to indirect imaging of difficult-to-access samples. Our wQGI scheme uses a commercially available multicore imaging fiber bundle, compatible with standard minimally invasive microendoscopy. Moreover, we use a single-photon avalanche diode (SPAD) image sensor specifically designed for QGI, with in-pixel asynchronous correlation logic [36,37]. Previous QGI experiments required bulky image-preserving optical delay lines [38] or offline coincidence post-processing to extract a ghost image after measurement completion [39,40]. In contrast, our image sensor's in-pixel correlation capability enables acquiring true real-time QGI videos without further system latency, using a simple optical setup. This makes live alignment possible, as well as rapid variation of acquisition parameters.

Here, we demonstrate our wQGI system to obtain high-quality images of a test sample at high speed, up to ∼Hz imaging rates. We also compare wQGI performance to standard direct free-space illumination QGI, quantifying differences in spatial resolution and photon losses, and discuss potential future improvements. Our work opens up the prospect of QGI applications in the bio-medical field, potentially enabling ultralow-light *in vivo* imaging of sensitive biological samples at wavelengths where suitable image sensors are not available.

## 2. WAVEGUIDED QUANTUM GHOST IMAGING

A conceptual overview of the proposed waveguided quantum ghost imaging (wQGI) scheme is shown in Fig. 1(a). The three insets show closeups of conjugate transverse planes: the anti-correlated photon pair illumination (left), the image sensor plane (centre), and the sample plane (right). Our quantum light source emits

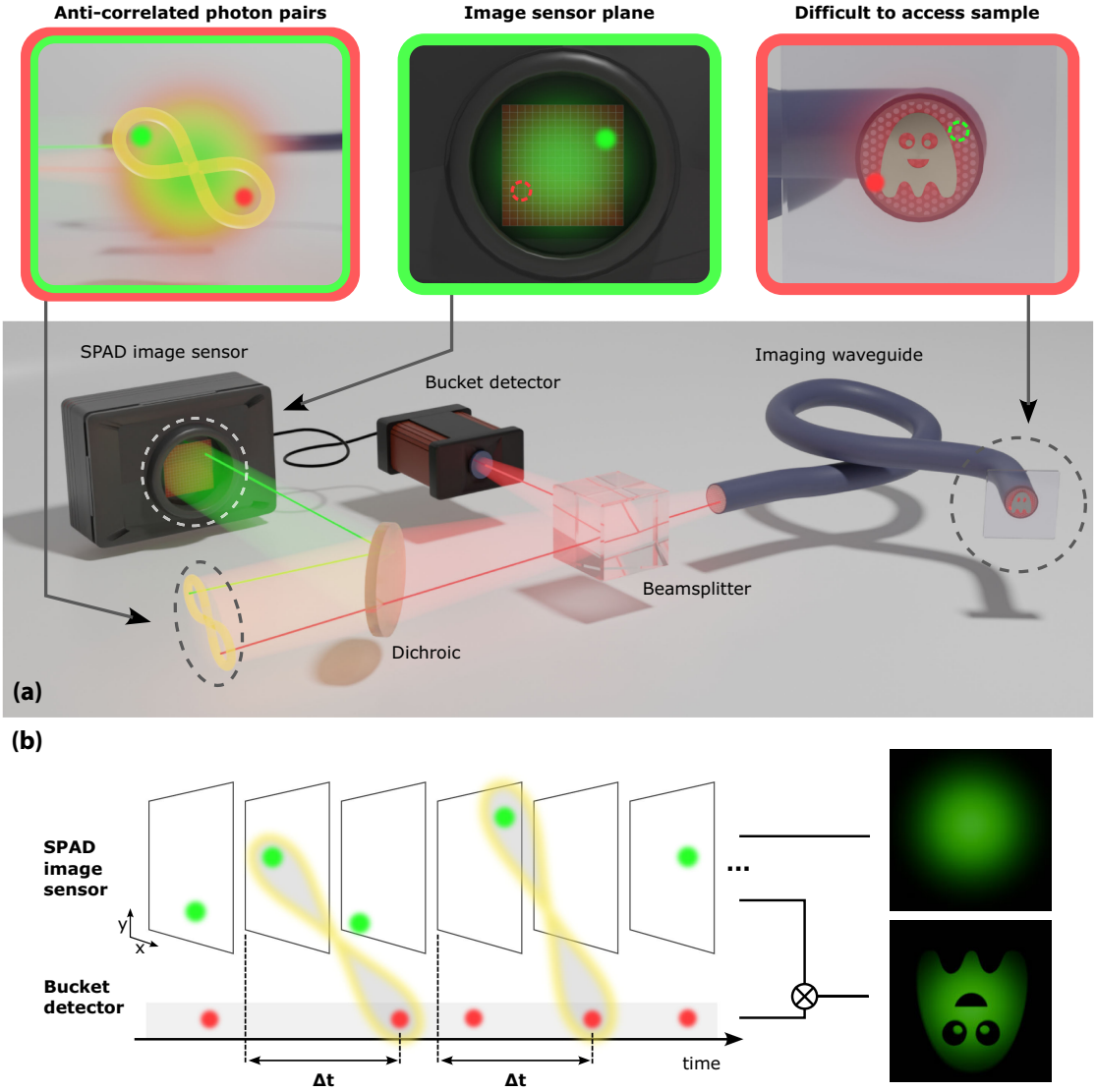


**Fig. 1.** Schematic overview of the experiment. (a) We separate photon pairs exhibiting spatiotemporal quantum correlations. With a SPAD image sensor array, we image one photon (signal, depicted as green) with spatial resolution. The other photon (idler, red) illuminates a sample through a waveguide and is registered with a bucket detector (single SPAD). (b) The SPAD image sensor correlates the two photons' asynchronous detections and constructs the quantum ghost image.

non-degenerate (two-color) photon pairs via SPDC, producing spatially anti-correlated photons in the shown far-field (FF), i.e., the Fourier plane of the source. The signal is drawn in green, and the idler in red. An example of an anti-correlated photon pair is shown as two dots in the left inset, while the example trajectories are represented by the solid lines in Fig. 1(a).

Photons from each pair are separated with a dichroic mirror. Signal photons are relayed directly onto the SPAD image sensor array (lenses not shown for simplicity), allowing measurement of both their positions and arrival times. A closeup of the image sensor detection plane appears in the centre inset of Fig. 1(a): the green dot indicates the position of the detected example signal, while the dashed red circle marks the position of its paired idler photon in the sample plane.

The idler photon is relayed onto the proximal end of a flexible imaging waveguide and propagated through it, probes a reflective sample [the ghost in Fig. 1(a)] placed in contact with the waveguide's distal end, and then passes back through the waveguide, being received by a single-pixel "bucket" detector. At the sample plane, the idler remains anti-correlated with the signal photon detected by the SPAD imager, as shown in the right inset: here, the red dot indicates the position of the example signal photon at the sample, and the dashed green circle indicates the position of its corresponding signal photon at the image sensor plane. Thus, rather than relaying an intensity image to the camera (distal to proximal), the bundle delivers the spatial quantum correlations to the sample (proximal to distal), with image reconstruction performed remotely from coincidences.

Figure 1(b) illustrates how the quantum ghost image of the sample is retrieved via asynchronous correlation. The imager records both position (x and y) as well as the time of the signal photon detections, with six example temporal slices shown. Corresponding idler photons [with real SPDC photon pairs indicated by yellow $\infty$ in Fig. 1(b)], due to traversing a longer optical path, are measured at a later moment in time (with temporal difference $\Delta t$) by the bucket detector.

If we sum over all detections on the SPAD image sensor without considering the bucket detector, no sample information can be gained, and only the Gaussian envelope of the illumination beam is seen. In contrast, by integrating over only the correlated photon detections for an inter-photon delay of $\Delta t$, we obtain an image of the sample. This is illustrated by the inverted ghost in Fig. 1(b), where the inversion follows from the spatial anti-correlation between the signal and the idler [14].

## 3. OPERATION PRINCIPLES OF wQGI

SPDC produces photon pairs, quantum correlated in position and momentum, through conversion in a bulk nonlinear crystal of pump photons with wavelength $\lambda_p$ into signal–idler pairs, with respective wavelengths $\lambda_s$ and $\lambda_i$. We will model here the implementation of QGI using SPDC momentum correlation. In transverse wavevector space, the non-classical two-photon wavefunction for signal–idler photon pairs can be written as

$$\Psi(\mathbf{k}_s^{\perp}, \mathbf{k}_i^{\perp}) = \frac{\sigma_+\sigma_-}{\pi} \exp\left[-\frac{\sigma_+^2}{4}|\mathbf{k}_s^{\perp} + \mathbf{k}_i^{\perp}|^2 - \frac{\sigma_-^2}{4}|\mathbf{k}_s^{\perp} - \mathbf{k}_i^{\perp}|^2\right]. \tag{1}$$

Here, $\mathbf{k}_{s,i}^{\perp}$ denotes the transverse momentum of the signal/idler, respectively. $\sigma_+$ corresponds to the waist of the Gaussian pump beam, and $\sigma_- = \sqrt{\alpha L \lambda_p / 2\pi}$, where $\alpha = 0.455$ is an adjustment constant, and $L$ is the nonlinear crystal's length [41]. The momentum anti-correlation strength is given by $\sigma_+^{-1}$, that is, the inverse of the pump beam waist. As $\sigma_+/\sigma_- \gg 1$ for SPDC sources, the exponential in Eq. (1) is dominated by its first term [42].

In our implementation, the signal and idler photons are separated and both projected into the FF of the SPDC generation zone via optical systems with respective effective focal lengths of $f_{s,i}$. This results in a mapping of transverse wavevectors $\mathbf{k}_{s,i}^{\perp}$ onto FF spatial locations $\mathbf{r}_{s,i}$ according to $\mathbf{k}_{s,i}^{\perp} = \beta_{s,i}\mathbf{r}_{s,i}$, where $\beta_{s,i} = 2\pi/(\lambda_{s,i} f_{s,i})$ is the conversion factor from momentum to FF position.

In the general case, the respective imaging systems for the signal and idler arms can be characterized through point-spread functions (PSFs) with non-zero widths $\sigma_{PSF,s}$ and $\sigma_{PSF,i}$. Then, we can express the resulting two-photon distribution between the signal in the image sensor plane and the idler in the sample plane as follows (full derivation in Supplement 1, Sections 1A and 1B):

$$\Psi_{\text{Sensor-Sample}}(\mathbf{r}_s, \mathbf{r}_i) \approx N \exp\left[\frac{-1}{4\underbrace{((\beta_s\sigma_{PSF,s})^2/2 + (\beta_i\sigma_{PSF,i})^2/2 + (\sigma_+^{-1})^2)}_{\sigma_{\text{eff}}^2}}|\beta_s\mathbf{r}_s + \beta_i\mathbf{r}_i|^2\right]. \tag{2}$$

We can express the conditional probability of detecting the idler at coordinates $\mathbf{r}_{\text{idler}}$, given a coincident signal detection at coordinates $\mathbf{r}_s$ as $|\Psi_{\text{Sensor-Sample}}(\mathbf{r}_s|\mathbf{r}_i)|^2$. This implies that $\mathbf{r}_i$ can be inferred, to some precision, by measuring $\mathbf{r}_s$ instead—the principle of QGI. The precision of this inference, and ultimately the spatial resolution of a quantum ghost image, is thus limited by $\sigma_{\text{eff}}$ (Eq. 2). Note that $\sigma_{\text{eff}} \to 0$ (perfect correlation) would imply $\mathbf{r}_i = -\beta_s/\beta_i \cdot \mathbf{r}_s$. In our wQGI scheme, the signal is relayed directly onto an image sensor, such that $\sigma_{PSF,s} \approx 0$, while the idler photon's FF plane illuminates the sample via an imaging system with a PSF with $\sigma_{PSF,i} \gg \sigma_{PSF,s}$. Therefore, we have $\sigma_{\text{eff}} \approx \sqrt{(\beta_i\sigma_{PSF,i})^2/2 + (\sigma_+^{-1})^2}$.

We model the spatially varying sample as an arbitrary function of lateral position $S(\mathbf{r}_i)$, where $0 \le S \le 1$, and $S(\mathbf{r}_i') = 1$ indicates that all light is reflected by the sample (when imaging in reflection) or transmitted (imaging in transmission). The quantum ghost image is then formed by detecting coincidences between the signal photon at a given spatial coordinate $\mathbf{r}_s'$, and a bucket detection of the idler, i.e., integrating over all $\mathbf{r}_i$ (details in Section 1C of Supplement 1):

$$\begin{aligned}\text{QGI}(\mathbf{r}_s') &= \int |\Psi_{\text{Sensor-Sample}}(\mathbf{r}_s', \mathbf{r}_i) S(\mathbf{r}_i)|^2 d\mathbf{r}_i \\ &= \frac{|N|^2}{\beta_i^2}\left[G_{\sigma_{\text{eff}}} * S_{\text{scaled}}^2\right](\beta_s\mathbf{r}_s'),\end{aligned} \tag{3}$$

where $G_{\sigma_{\text{eff}}}$ is a Gaussian function with width $\sigma_{\text{eff}}$, $*$ represents a convolution, and $S_{\text{scaled}}^2(\mathbf{r}) = S^2(\mathbf{r}/\beta_i)$. That is, the quantum ghost image yields exactly a scaled image of the sample $S$, blurred by the momentum correlation strength $\sigma_+^{-1}$ and the idler optical system PSF $\sigma_{PSF,i}$.

In practice, $\sigma_+^{-1}$ can be measured directly by detecting signal–idler coincidences in the same FF plane, and $\sigma_{PSF,i}$ can be estimated

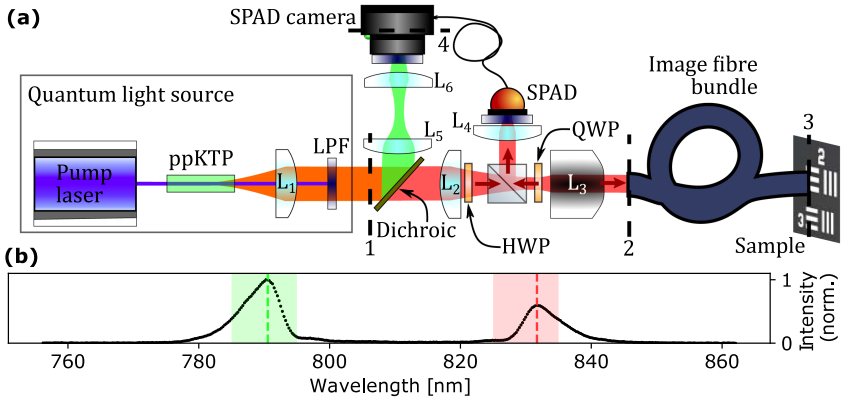


**Fig. 2.** (a) Experimental setup. Non-degenerate photon pairs generated via SPDC in a ppKTP crystal exhibit spatial anti-correlation in the crystal FF, indicated by dashed line 1. The pump is removed through a long-pass filter (LPF). The photon pairs are then separated by a dichroic mirror into the signal and idler beams. The signal (depicted as green) is relayed directly to the SPAD image sensor array (plane 4). The idler (red) is routed through a half-wave plate (HWP), polarizing beam splitter (PBS), and quarter-wave plate (QWP), then demagnified onto the proximal facet of a flexible imaging fiber bundle (plane 2), transmitted to the distal facet (plane 3, reflective sample), and returns via the same fiber. Upon return, the QWP and PBS direct the idler to a bucket detector (SPAD). (b) Spectrum of the non-degenerate SPDC source. Different peak heights are due to the wavelength-dependent quantum efficiency of the spectrometer. Vertical dashed lines indicate the approximate centre wavelengths of the signal (790 nm, green) and the idler (830 nm, red). Shaded areas indicate wavelengths bands used.

by sending both the signal and the idler through the same imaging system [35]. This is described in Sections 1D and 2B of Supplement 1.

## 4. EXPERIMENTAL REALIZATION OF wQGI

Our wQGI scheme comprises three main components: a quantum light source, an optical system including an image-preserving waveguide (fiber bundle), and a detection system consisting of a custom SPAD image sensor array and a bucket single-photon detector. Figure 2(a) presents an overview of the full experimental setup. In this section, we detail the implementation and performance of each subsystem.

### A. Quantum Light Source

Our quantum light source produces non-degenerate photon pairs in a bulk nonlinear crystal through SPDC, as shown in Fig. 2(a). We pump with a continuous-wave single-mode laser (Omikron) at $\lambda_p \approx 405$ nm, coupled into a single-mode fiber (Thorlabs SM400), collimating (Thorlabs F671FC-405) the fiber output to a beam diameter of 0.6 mm with 2.5 mW of optical power. The collimated pump beam passes through a periodically poled potassium titanyl phosphate (ppKTP) crystal (Raicol, 2 mm × 1 mm × 20 mm), which is maintained at approximately 56.3°C by a resistive oven (Covesion) in order to satisfy the type-0 non-degenerate phase-matching condition. Pump, signal, and idler photons are all vertically (V) polarized and satisfy the energy conservation condition:

$$\frac{1}{\lambda_p} = \frac{1}{405\ \text{nm}} = \frac{1}{\lambda_s} + \frac{1}{\lambda_i}. \tag{4}$$

Figure 2(b) shows the measured SPDC spectrum (OceanOptics HDX), and we select $\approx 10$ nm bandwidths centered on $\lambda_s \approx 790$ nm and $\lambda_i \approx 830$ nm. Note that, in future work, the idler wavelength can be extended further into the infrared.

After the crystal, the pump is rejected using a long-pass filter (Thorlabs FELH0750), and both the signal and the idler are collected by a lens with a focal length $f_1 = 175$ mm. Plane 1 in Fig. 2(a) corresponds to the generation FF $f_1$ after the collecting lens. The photon pairs are then split deterministically, with a dichroic mirror (longpass, Chroma T810lpxr), into separate signal and idler beams.

### B. Optical System

The idler beam's polarization is rotated by a half-wave plate (Thorlabs WPH10M-830), such that it passes through a polarizing beam splitter cube (Thorlabs PBS255), followed by a quarter-wave plate (Thorlabs WPQ10M-830) oriented at 22.5°. With a telescope comprising a lens with a focal length $f_2 = 400$ mm and a 10× microscope objective ($f_3$, Thorlabs MY10X-823), we demagnify the source FF—plane 1 in Fig. 2(a)—onto the fiber proximal facet, plane 2. We use a commercially available flexible imaging fiber bundle (Fujikura FIGH-10-500N, 30 cm, bent in loops) with an outer diameter (including jacket) of 600 µm and an image circle diameter of 460 ± 25 µm. The fiber has a total of around 10,000 cores, with a ∼2.9 µm diameter and refractive indices of 1.5—compared to 1.446 for the cladding [31]—such that propagation modes are guided through total internal reflection. The cores are arranged in an approximately hexagonal pattern, with a core-to-core spacing of ∼4.5 µm. From the refractive indices, the numerical aperture can be calculated to be 0.39. Idler photons propagate through this imaging fiber bundle from its proximal to distal end, which is in contact with a reflective sample. That is, the fiber transmits the spatial correlations from plane 2 to plane 3 in Fig. 2(a).

After reflection from the sample, the idler photons are recoupled into the fiber bundle and transmitted back to the proximal facet. The returning beam is collimated by the same microscope objective, and, after a second pass through the quarter-wave plate, its polarization is rotated to vertical. This ensures that the beam is now reflected by the PBS and focused by a lens ($f_4 = 11$ mm) onto the active area of the bucket detector.

The signal beam, on the other hand, is imaged directly onto the image sensor via a telescope comprising lenses with focal lengths

$f_5 = 500$ mm and $f_6 = 150$ mm. That is, we relay the signal photons from plane 1 [Fig. 2(a)], onto the sensor, plane 4. We also calculate the magnification $M$ between the idler and signal beam and thus obtain the correct feature size of the ghost image (the idler beam), where $\beta_{s,i}$ are defined in Section 3:

$$M = \frac{\beta_s}{\beta_i} = \underbrace{\frac{\lambda_i}{\lambda_s}}_{\text{spectrum}} \underbrace{\frac{f_5/f_6}{f_2/f_3}\frac{f_1}{f_1}}_{\text{optical .system}}. \tag{5}$$

### C. Detection System

Detection in our wQGI setup is performed via two single-photon sensitive devices: a "bucket" detector for the idler photons and an image sensor for the signal photons. The idler photons are registered by a single-pixel SPAD module (Excelitas SPCM-AQRH-13), featuring a photon detection efficiency (PDE) of 54% at 850 nm. Upon detection, each idler photon produces an electrical pulse that is routed via coaxial cable to the SPAD image sensor array. This custom SPAD-based imager, recently proposed by Gandola *et al*. for QGI applications [36], captures the signal photons. For full details on the sensor architecture, we refer the reader to the cited paper. The sensor array consists of 100 × 100 pixels with a 17 μm pitch and two halves with different architectures, resulting in fill factors of either 19% or 31% [36]. In our experiment, we exclusively use the area with the higher fill-factor architecture, due to its higher PDE (≈ 2.5% at 810 nm, with 3 V excess bias voltage). To increase the frame rate and minimize dead-time caused by the image sensor readout process, a row-level skip logic has been implemented to bypass empty rows. This technique is particularly beneficial in photon-starved conditions, which are typical of ghost imaging applications, ensuring fast sensor readout and real-time operation.

To identify photon coincidences between the signal photons—detected by each pixel, and the bucket electrical pulses—arriving asynchronously, the SPAD image sensor performs in-pixel time correlation. For that, each pixel can electronically delay the digitized SPAD front-end output, compensating for the constant temporal offset between both the signal and the idler. Therefore, after the set delay, only the pixel detections overlapping with bucket events within a user-definable correlation window (≈ 5 ns in our experiment, significantly larger than any expected mode dispersion effects in 2 × 30 cm fiber propagation) are stored in a 1-bit in-pixel memory for readout. That is, the idler-gated coincidence image is directly calculated in-sensor, avoiding the need to post-process detection timestamps on an external computer. Also, this approach avoids image-preserving delay lines, which is even more important in wQGI than for standard free-space QGI, as the idler's propagation back and forth through the imaging fiber adds additional temporal offset. The resulting real-time visual feedback also significantly speeds up alignment of the quantum light source and optical system introduced above, as well as optimization of the acquisition parameters——such as delay time and correlation window.

There are several sources of noise in our QGI measurements. First, accidental coincidences can result from uncorrelated signal and idler photons being registered within the SPAD image sensor correlation window. Second, dark counts in the image sensor and bucket detector, as well as stray ambient light, add background noise to the raw measured image. A disproportional part of the dark counts stems from a few individual pixels (so-called hot pixels), adding spatially highly non-uniform noise. In our work, we mitigate all these sources of noise, optimizing for image SNR. This is described in detail in Section 3 of Supplement 1.

## 5. RESULTS

To demonstrate the capabilities of our wQGI scheme, we performed imaging measurements of a reflective test sample: a microscopy slide sputtered with a gold pattern (USAF 1951 resolution test target). We compare wQGI to standard, free-space QGI. For both imaging modalities, we present high-resolution quantum ghost images and study possible imaging rates.

### A. Waveguided Quantum Ghost Imaging

In Figs. 3(a) and 3(e), we show quantum ghost images acquired through our image-preserving waveguide, corresponding to scenarios where the sample is inaccessible for direct imaging—for example, hard to reach or occluded from direct view. The reflective sample was placed at the distal end of the waveguide—plane 3 as defined in Fig. 2(a). The field of view is ∼200 μm, and the total measurement time in both cases was around 20 min per image. Despite the absence of distal magnification optics, features at the few-μm scale are accurately reproduced in both Fig. 3(a) (USAF 1951 group 4, element 3: line width 24.80 μm) and Fig. 3(e) (USAF 1951 group 5, elements 4 and 5: line widths 11.05 and 9.84 μm, respectively). Moreover, as can be seen in the cross-section plots in Figs. 3(c) and 3(g), our wQGI system provides high SNR. We evaluated the SNR for the retrieved ghost images (see Section 3 in Supplement 1), defining regions of interest for a sample feature (signal) and the image background (noise). We indicate these regions of interest by black (feature) and white (background) rectangles, respectively, in Fig. 3. We obtain SNR values of $12.4 \pm 4.2$ for the larger features [Fig. 3(a)] and $5.4 \pm 1.7$ for the smaller features [Fig. 3(e)]. Dividing the total number of detected coincidences that form quantum ghost images in Figs. 3(a) and 3(e) by the acquisition time yields coincidence rates of $4.6 \times 10^4$ and $3.7 \times 10^4$ s$^{-1}$, respectively. In Figs. 3(b) and 3(f), we imaged the same respective sample regions as in Figs. 3(a) and 3(e) but without the waveguide, corresponding to a standard QGI scheme [sample placed where in wQGI at plane 2 as defined in Fig. 2(a)]. Comparing Figs. 3(a) and 3(e) to Figs. 3(b) and 3(f) shows that the image fiber bundle introduces resolution loss. This is also confirmed by the cross-sections in Figs. 3(d) and 3(h), which exhibit slightly better resolution and higher image contrast when compared to Figs. 3(c) and 3(g). As, fundamentally, in QGI, the image resolution is limited by the spatial anti-correlation (compare Eq. 3), we attribute the reduced resolution to a decrease in correlation strength caused by our image-preserving waveguide. To quantitatively confirm the waveguide's effect on the quantum correlations, those can be measured before and after the waveguided imaging system (see Section 1D in Supplement 1) [35]. Full experimental details can be found in Section 2A of Supplement 1. From the results of this quantum correlation measurement, we expect a PSF characterized by $\sigma_{\mathrm{PSF,i}} = 3.30$ μm for our wQGI imaging scheme. This resolution loss—comparable to the image pixel size of 3 μm—is consistent with the QGI results: in Fig. 3, the group 5, element 5 bars (9.84 μm) are resolved in both columns, albeit with reduced contrast in the waveguided case, Fig. 3(e).

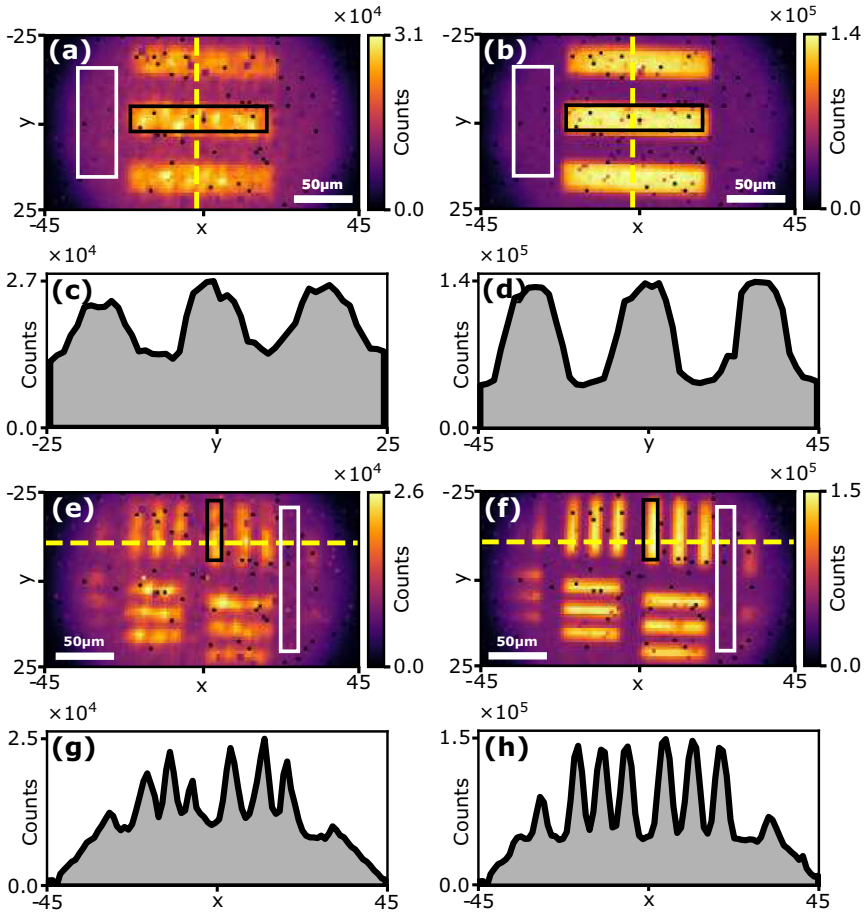


**Fig. 3.** Quantum ghost imaging results. Left column: wQGI, right column: direct, free-space QGI. (a) and (b) USAF 1951 group 4, element 3, sample placed at plane 3 for (a), plane 2 for (b), as shown in Fig. 2(a). Measurement times ∼20 min. (c), (d) Cross-sections along yellow dashed lines in (a) and (b). (e)–(h) Equivalent to (a)–(d), with the sample USAF 1951 group 5, elements 4 and 5. Black (white) rectangles in (a), (b), (e), (f) represent signal (background) region of interest for the SNR calculation. The color map encodes the number of photon coincidences accumulated per pixel.

Furthermore, the SNRs in free-space QGI are $18.1 \pm 4.7$ [Fig. 3(b)] and $9.0 \pm 2.8$ [Fig. 3(f)], that is, 1.46 and 1.67 times higher than for Figs. 3(a) and 3(e), respectively. The coincidence rates for the direct imaging QGI case [Figs. 3(b) and 3(f)] were calculated to be $2.0 \times 10^5\ s^{-1}$, implying an excess loss of 6.38 to 7.3 dB induced by the waveguided imaging system.

### B. Imaging Rate

Lastly, we investigated the potential of our wQGI system for high-speed, or even real-time, endoscopic imaging applications. We reduced the image acquisition time from 120 s, as shown in Fig. 4(a), to 12 [Fig. 4(b)], 1.2 [Fig. 4(c)], and 0.12 s [Fig. 4(d)]. As expected, image quality, as well as SNR, reduces with acquisition time, but we see that approximately 1 s is already sufficient to discern binary sample features. Therefore, our experimental system enables ∼Hz rate real-time non-invasive quantum ghost imaging, albeit at relatively low SNR. Moreover, we see from Fig. 4(b) that acquisition times of a few seconds suffice to obtain high-quality images.

Equivalently, we varied image acquisition time for the free-space QGI system—without waveguide—as well, as shown in Figs. 4(e)–4(h). From that, we can see that in this case, even shorter acquisition times are possible. To demonstrate our QGI system's real-time capability, we recorded live screen captures of the SPAD camera's graphical user interface while translating the fiber's proximal facet (waveguided) or the sample (free space) using manual stages. These QGI videos—Visualization 1 and Visualization 2, for the waveguided and free-space case, at 1 and 2.5 Hz, respectively—clearly show the sample moving in real time.

## 6. DISCUSSION

We have demonstrated waveguided quantum ghost imaging (QGI) through a commercially available image-preserving fiber bundle, combined with a custom SPAD-based image sensor that performs in-pixel asynchronous correlation for real-time image acquisition.

The present waveguided QGI (wQGI) setup exceeds a spatial resolution of 9.8 μm without magnification optics at the waveguide's distal end, with USAF group 5, element 5 features clearly resolved. We obtained SNRs up to $12.4 \pm 4.2$ for larger test features (group 4, element 3, 24.8 μm), with acquisition times on the order of 1.2 s sufficient to render binary features visible (see Fig. 4). The coincidence rate in this waveguided configuration was $4.6 \times 10^4\ s^{-1}$: thus, around $5 \times 10^4\ s^{-1}$ detected coincidences, which are sufficient to visualize an occluded sample, demonstrating low-light imaging through a waveguide.

These results directly address the need, outlined in Section 1, for imaging modalities capable of visualizing regions inaccessible to

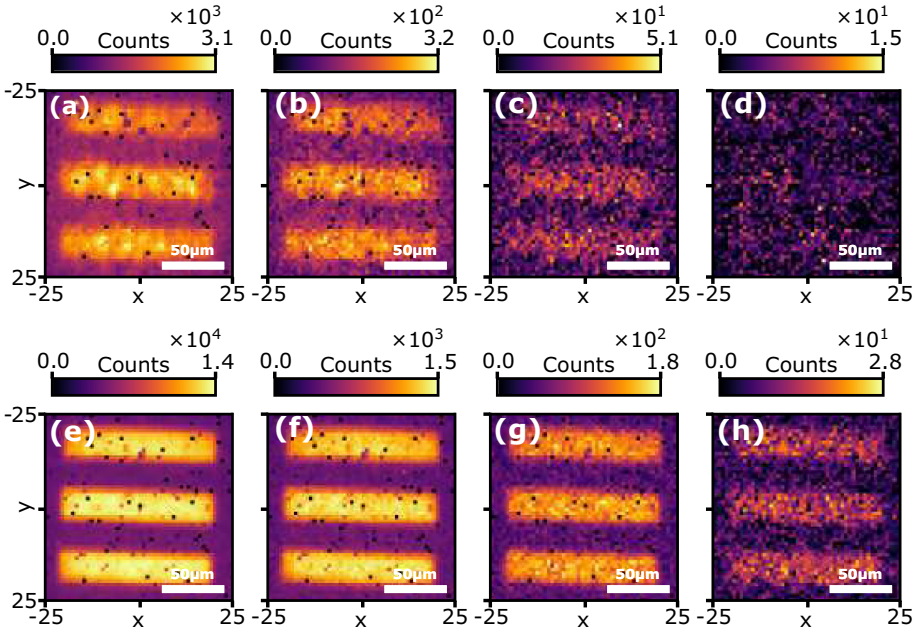


**Fig. 4.** Quantum ghost imaging results. (a)–(d) Equivalent to Fig. 3(a), (e)–(h) equivalent to Fig. 3(b), but with measurement times 120, 12, 1.2, and 0.12 s, respectively. The color map encodes the number of photon coincidences accumulated per pixel.

direct imaging—such as internal tissues in endoscopy or confined industrial environments—while operating at low light levels. Even though the proof-of-principle demonstration in this work was performed in non-degeneracy with a small wavelength difference, future work will focus on two-color wQGI with the idler in the infrared, a wavelength range where camera technological maturity is low. Such applications are enabled by combining highly non-degenerate SPDC sources [43] with commercially available MIR bucket detectors and suitable optical waveguides: appropriate candidates include fiber bundles for NIR [33,44] and MIR [45].

We note that the performance of our wQGI system can further be improved beyond the results shown here, through optimization of its three main components: the quantum light source, the optical system (including the waveguide/image fiber bundle), and the detectors (the SPAD image sensor and the bucket detector).

The source correlation strength $\sigma_{+,\mathrm{in}}^{-1}$ generally defines spatial resolution in a standard free-space QGI experiment. Tailoring the SPDC source allows for optimizing these correlations [46]. In our setup, $\sigma_{+,\mathrm{in}}^{-1}$ can be further increased in a straightforward manner by employing a ppKTP crystal shorter than the current 20 mm; the resulting reduced photon flux could be mitigated, for example, by higher pump power.

Optical losses in the waveguided imaging system can be reduced significantly in two main ways: first, by adding a microlens array to enhance coupling efficiency into the fiber bundle [47], and second, by selecting optics with sufficiently high numerical aperture. Resolution degradation in the image fiber arises from pixelation and cross-talk (undesired coupling between adjacent modes). By analyzing spatial correlations between photon pairs, we found that the average effect of transporting one photon of a pair through the fiber is well-described by a Gaussian PSF with a standard deviation of 3.30 μm, comparable to the 4.50 μm core-to-core spacing. In the wQGI images, Figs. 3(a) and 3(e), several bright spots—which correspond to fiber bundle cores' modes—are visible. The core-to-core spacing is, in particular for small features such as in Fig. 3(e), on the order of magnitude of the feature size. Thus, the mode density fundamentally limits the resolution achievable without additional distal optics, such that higher mode density is warranted. Conventional image fiber bundles are limited by a trade-off: increasing pixel density also increases cross-talk, which typically restricts the mode density to around 0.1 modes/μm$^2$ [32,48]. Recent fiber bundle designs use randomness to reduce cross-talk [33,44,49]. Even more randomness may yield further benefits, such as in transverse Anderson localization optical fiber (TALOF) [50]. TALOF has a disordered transverse cross-section, from which transversely localized modes originate. Relying on these localized modes instead of conventional cores to guide light, TALOF can minimize both cross-talk and pixelation [51], achieving up to 100 times higher mode density, and reaching 10 modes/μm$^2$ [52]. Hence, Anderson localization fiber can transmit images with similar or superior quality compared to conventional bundles over meter-scale distances [51,53] and has also been developed for NIR [54,55] or MIR [56] transmission. We note that our wQGI method is also fully compatible with endoscopy schemes using multimode fibers as the image-transmitting waveguide [57]. However, this requires (in contrast to wQGI with an image fiber bundle or Anderson localization fiber), active transfer-matrix calibration and realignment using, for example, spatial light modulators.

SPAD image sensors are an active area of research and development, with performance improving rapidly. To increase photon detection probability, one approach is to increase the fill factor, typically via microlens arrays or, more recently, 3D stacking of microelectronics for QGI-specific image sensors [58]. A new 472 × 456 SPAD image sensor, which is an evolution of the one used in this work [36], is currently undergoing characterization. To maintain high frame rates despite the 20× larger matrix, address-based pixel readout was implemented, and the skipping mechanism was extended to the column level. Our wQGI technology may also enable further advanced imaging capabilities, including adding depth resolution to create 3D images, either through aperture filtering [59] or by leveraging the improving

time resolution of SPAD imagers [60]. So far, a depth resolution of about 10 cm has been reported [61]. Future time-to-digital converters with a precision below 10 ps [62] may also deliver mm-scale depth resolution. This methodology holds promise for imaging volumetric and photosensitive samples, such as biological tissues.

Overall, we have shown that the current system resolution is limited by the source correlation strength and mode density in the commercial fiber bundle. The detected photon pair rate is limited primarily by the SPAD image sensor's photon detection probability. Integration of higher-density fiber bundles and next-generation SPAD imagers can improve significantly image both resolution and acquisition speed.

## 7. CONCLUSION

We have demonstrated scanning-free, real-time waveguided imaging at the single-photon level, achieved through quantum ghost imaging implemented with a commercial flexible optical fiber bundle and a custom SPAD image sensor. Our system enables high-resolution image reconstruction (pixel size 3 μm) of occluded samples with minimal invasiveness and operates under ultralow-light conditions, evidenced by successful imaging at detected coincidence rates below $5 \times 10^4\ s^{-1}$. The platform does not require any active optical modulation or scanning, and on-chip correlation in the SPAD imager eliminates the need for optical delay lines and post-processing, allowing a highly compact and latency-free practical real-time imaging setup.

Employing the fiber bundle to deliver quantum correlations to the sample allows us to extend the benefits of quantum imaging to minimally invasive applications, where conventional free-space imaging systems are unsuitable—such as biomedical endoscopy, remote industrial inspection, or any environment where direct access and high illumination are impractical or potentially damaging. In particular, the low-light operation is crucial for imaging sensitive biological tissue, for reducing photodamage, or for scenarios with strict photon budgets or high background noise. Furthermore, the demonstrated scheme provides a route toward imaging at exotic wavelengths (e.g., infrared) by combining highly non-degenerate photon-pair sources with appropriate waveguides and detectors.

More generally, this work may motivate further experiments in the future combining the use of waveguides and quantum light.

Ongoing advances in quantum light sources, image fiber, and high-speed SPAD imagers will further increase the spatial resolution, speed, and versatility of this platform, enabling robust imaging across a broad range of applications where low-light performance, illumination wavelength, and access constraints are critical.

**Funding.** Agencia Estatal de Investigación (CEX2024-001490-S, MICIU/AEI/10.13039/501100011033, MCIN/AEI/10.13039/501100011033/FEDER); Fundación Cellex (ICFO CELLEX PhD-fellowship); FUNDACIÓ Privada MIR-PUIG; Centres de Recerca de Catalunya; Ministerio de Economía y Competitividad (MAGICAL: PID2022-137952NB-I00); Ministerio de Ciencia, Innovación y Universidades (PRTR-C17.I1); H2020 Future and Emerging Technologies (899580, H2020-FETOPEN-2018-2020); HORIZON EUROPE Digital, Industry and Space (101082596, PROMISE: 101189611, HILIGHT: 101135034); Ministero dell'Istruzione, dell'Università e della Ricerca (PNRR MUR project, PE23-NQSTI).

**Acknowledgment.** The authors would like to acknowledge Javier Arrés Chillón for fabricating the test sample, as well as Prof. Federica Villa and the SPADlab at Politecnico di Milano and Micro Photon Devices s.r.l. for providing the 24 × 24 SPAD image sensor. This work was partially funded by Agencia Estatal de Investigación, Fundació Cellex, Fundació Mir-Puig, and Generalitat de Catalunya through CERCA. A. D. acknowledges support of the ICFO CELLEX PhD-fellowship. R.C. acknowledges funding from the European Union's Horizon Europe research and innovation programme (QUDICE). We thankfully acknowledge the financial support from the European Commission through the Grant Agreement No. 899580 (project "FastGhost"), No. 101189611 (project PROMISE) and No. 101135034 (project HILIGHT), and the Italian Ministry of University and Research through the PNRR MUR project PE23-NQSTI.

**Disclosures.** The authors declare no conflicts of interest.

**Data availability.** Data underlying the results presented in this paper are not publicly available at this time but may be obtained from the authors upon reasonable request.

**Supplemental document.** See Supplement 1 and Visualization 1 and Visualization 2 for supporting content.

## REFERENCES

1. P.-A. Moreau, E. Toninelli, T. Gregory, *et al.*, "Imaging with quantum states of light," Nat. Rev. Phys. **1**, 367–380 (2019).
2. M. Gilaberte Basset, F. Setzpfandt, F. Steinlechner, *et al.*, "Perspectives for applications of quantum imaging," Laser Photonics Rev. **13**, 1900097 (2019).
3. C. A. Casacio, L. S. Madsen, A. Terrasson, *et al.*, "Quantum-enhanced nonlinear microscopy," Nature **594**, 201–206 (2021).
4. M. Unternährer, B. Bessire, L. Gasparini, *et al.*, "Super-resolution quantum imaging at the Heisenberg limit," Optica **5**, 1150–1154 (2018).
5. H. Defienne, P. Cameron, B. Ndagano, *et al.*, "Pixel super-resolution with spatially entangled photons," Nat. Commun. **13**, 3566 (2022).
6. G. Brida, M. Genovese, and I. Ruo Berchera, "Experimental realization of sub-shot-noise quantum imaging," Nat. Photonics **4**, 227–230 (2010).
7. R. Camphausen, Á. Cuevas, L. Duempelmann, *et al.*, "A quantum-enhanced wide-field phase imager," Sci. Adv. **7**, eabj2155 (2021).
8. G. B. Lemos, V. Borish, G. D. Cole, *et al.*, "Quantum imaging with undetected photons," Nature **512**, 409–412 (2014).
9. H. Defienne, B. Ndagano, A. Lyons, *et al.*, "Polarization entanglement-enabled quantum holography," Nat. Phys. **17**, 591–597 (2021).
10. S. Töpfer, M. Gilaberte Basset, J. Fuenzalida, *et al.*, "Quantum holography with undetected light," Sci. Adv. **8**, eabl4301 (2022).
11. T. B. Pittman, Y. Shih, D. Strekalov, *et al.*, "Optical imaging by means of two-photon quantum entanglement," Phys. Rev. A **52**, R3429 (1995).
12. D. Strekalov, A. Sergienko, D. Klyshko, *et al.*, "Observation of two-photon "ghost" interference and diffraction," Phys. Rev. Lett. **74**, 3600 (1995).
13. A. Anwar, C. Perumangatt, F. Steinlechner, *et al.*, "Entangled photon-pair sources based on three-wave mixing in bulk crystals," Rev. Sci. Instrum. **92**, 041101 (2021).
14. M. J. Padgett and R. W. Boyd, "An introduction to ghost imaging: quantum and classical," Philos. Trans. R. Soc. A **375**, 20160233 (2017).
15. T. Pittman, D. Strekalov, D. Klyshko, *et al.*, "Two-photon geometric optics," Phys. Rev. A **53**, 2804 (1996).
16. K. W. C. Chan, M. N. O'Sullivan, and R. W. Boyd, "Two-color ghost imaging," Phys. Rev. A **79**, 033808 (2009).
17. R. S. Aspden, N. R. Gemmell, P. A. Morris, *et al.*, "Photon-sparse microscopy: visible light imaging using infrared illumination," Optica **2**, 1049–1052 (2015).
18. D. P. Ryan, K. Meier, K. Seitz, *et al.*, "Infrared quantum ghost imaging of living and undisturbed plants," Optica **11**, 1261–1267 (2024).
19. M. Razeghi and B.-M. Nguyen, "Advances in mid-infrared detection and imaging: a key issues review," Rep. Prog. Phys. **77**, 082401 (2014).
20. P. Wang, H. Xia, Q. Li, *et al.*, "Sensing infrared photons at room temperature: from bulk materials to atomic layers," Small **15**, 1904396 (2019).
21. J. H. Shapiro and R. W. Boyd, "The physics of ghost imaging," Quantum Inf. Process. **11**, 949–993 (2012).
22. M. N. O'Sullivan, K. W. C. Chan, and R. W. Boyd, "Comparison of the signal-to-noise characteristics of quantum versus thermal ghost imaging," Phys. Rev. A **82**, 053803 (2010).
23. A. Meda, E. Losero, N. Samantaray, *et al.*, "Photon-number correlation for quantum enhanced imaging and sensing," J. Opt. **19**, 094002 (2017).

24. Y. Fu, H. Wang, R. Shi, *et al.*, "Characterization of photodamage in coherent anti-Stokes Raman scattering microscopy," Opt. Express **14**, 3942–3951 (2006).
25. S. Wäldchen, J. Lehmann, T. Klein, *et al.*, "Light-induced cell damage in live-cell super-resolution microscopy," Sci. Rep. **5**, 15348 (2015).
26. D. C. Fernandez, R. Bhargava, S. M. Hewitt, *et al.*, "Infrared spectroscopic imaging for histopathologic recognition," Nat. Biotechnol. **23**, 469–474 (2005).
27. M. Hermes, R. B. Morrish, L. Huot, *et al.*, "Mid-IR hyperspectral imaging for label-free histopathology and cytology," J. Opt. **20**, 023002 (2018).
28. T. P. Wrobel and R. Bhargava, "Infrared spectroscopic imaging advances as an analytical technology for biomedical sciences," Anal. Chem. **90**, 1444–1463 (2018).
29. M. Gu, H. Bao, and H. Kang, "Fibre-optical microendoscopy," J. Microsc. **254**, 13–18 (2014).
30. Y. Kim, S. C. Warren, J. M. Stone, *et al.*, "Adaptive multiphoton endomicroscope incorporating a polarization-maintaining multicore optical fibre," IEEE J. Sel. Top. Quantum Electron. **22**, 171–178 (2015).
31. K. L. Reichenbach and C. Xu, "Numerical analysis of light propagation in image fibers or coherent fiber bundles," Opt. Express **15**, 2151–2165 (2007).
32. H. A. Wood, K. Harrington, J. M. Stone, *et al.*, "Quantitative characterization of endoscopic imaging fibers," Opt. Express **25**, 1985–1992 (2017).
33. H. A. C. Wood, K. Harrington, T. A. Birks, *et al.*, "High-resolution air-clad imaging fibers," Opt. Lett. **43**, 5311–5314 (2018).
34. J. Hordell, D. Benedicto-Orenes, P. G. Petrov, *et al.*, "Transport of spatial squeezing through an optical waveguide," Opt. Express **26**, 22783–22792 (2018).
35. A. Demuth, R. Camphausen, Á. Cuevas, *et al.*, "Quantum light transport in phase-separated Anderson localization fiber," Commun. Phys. **5**, 261 (2022).
36. M. Gandola, E. Manuzzato, M. Perenzoni, *et al.*, "A 100 × 100 CMOS SPAD array with in-pixel correlation techniques for fast quantum ghost imaging applications," in *IEEE 49th European Solid State Circuits Conference (ESSCIRC)* (IEEE, 2023), pp. 105–108.
37. E. Manuzzato, M. Gandola, M. Perenzoni, *et al.*, "Architectural modeling and experimental characterization of a SPAD-based imager developed for fast-quantum ghost imaging applications," in *Annual Meeting of the Italian Electronics Society* (Springer, 2024), pp. 228–237.
38. R. S. Aspden, D. S. Tasca, R. W. Boyd, *et al.*, "EPR-based ghost imaging using a single-photon-sensitive camera," New J. Phys. **15**, 073032 (2013).
39. C. Pitsch, D. Walter, S. Grosse, *et al.*, "Quantum ghost imaging using asynchronous detection," Appl. Opt. **60**, F66–F70 (2021).
40. V. F. Gili, D. Dupish, A. Vega, *et al.*, "Quantum ghost imaging based on a "looking back" 2D SPAD array," Appl. Opt. **62**, 3093–3099 (2023).
41. K. Chan, J. Torres, and J. Eberly, "Transverse entanglement migration in Hilbert space," Phys. Rev. A **75**, 050101 (2007).
42. D. S. Tasca, S. Walborn, P. H. S. Ribeiro, *et al.*, "Propagation of transverse intensity correlations of a two-photon state," Phys. Rev. A **79**, 033801 (2009).
43. M. Kumar, P. Kumar, A. Vega, *et al.*, "Mid-infrared photon pair generation in $AgGaS_2$," Appl. Phys. Lett. **119**, 244001 (2021).
44. F. Qu, B. Xu, F. Yu, *et al.*, "Bend-resistant high-resolution imaging optical fiber," Opt. Laser Technol. **157**, 108650 (2023).
45. A. Nakatani, M. Matsumoto, G. Sakai, *et al.*, "High-resolution mid-infrared image transport by a chalcogenide multi-core fiber," Jpn. J. Appl. Phys. **63**, 102001 (2024).
46. P.-A. Moreau, E. Toninelli, T. Gregory, *et al.*, "Ghost imaging using optical correlations," Laser Photonics Rev. **12**, 1700143 (2018).
47. X.-T. Yan, J.-F. Yang, B. Xue, *et al.*, "Design of the microlens arrays coupling with imaging fiber bundle," Optoelectron. Lett. **9**, 169–172 (2013).
48. X. Chen, K. L. Reichenbach, and C. Xu, "Experimental and theoretical analysis of core-to-core coupling on fiber bundle imaging," Opt. Express **16**, 21598–21607 (2008).
49. J. De Clermont-Gallerande, T. Suzuki, A. Nakatani, *et al.*, "Tellurite-based oxide fiber simulated beam pattern evolution using a refractive index network with controlled randomness," Opt. Fiber Technol. **79**, 103343 (2023).
50. S. Karbasi, C. R. Mirr, P. G. Yarandi, *et al.*, "Observation of transverse Anderson localization in an optical fiber," Opt. Lett. **37**, 2304–2306 (2012).
51. S. Karbasi, R. J. Frazier, K. W. Koch, *et al.*, "Image transport through a disordered optical fibre mediated by transverse Anderson localization," Nat. Commun. **5**, 3362 (2014).
52. X. Hu, J. Zhao, J. E. Antonio-Lopez, *et al.*, "Unsupervised full-color cellular image reconstruction through disordered optical fiber," Light Sci. Appl. **12**, 125 (2023).
53. J. Zhao, J. E. A. Lopez, Z. Zhu, *et al.*, "Image transport through meter-long randomly disordered silica-air optical fiber," Sci. Rep. **8**, 3065 (2018).
54. P. Roth, G. K. L. Wong, J. Zhao, *et al.*, "Wavelength dependence of transverse Anderson localization in disordered glass-air fiber," Proc. SPIE **11206**, 1120601 (2019).
55. T. H. Tuan, S. Kuroyanagi, K. Nagasaka, *et al.*, "Near-infrared optical image transport through an all-solid tellurite optical glass rod with transversely-disordered refractive index profile," Opt. Express **26**, 16054–16062 (2018).
56. A. Nakatani, H. T. Tong, M. Matsumoto, *et al.*, "Transverse Anderson localization of mid-infrared light in a chalcogenide transversely disordered optical fiber," Opt. Express **30**, 5159–5166 (2022).
57. D. Stellinga, D. B. Phillips, S. P. Mekhail, *et al.*, "Time-of-flight 3D imaging through multimode optical fibers," Science **374**, 1395–1399 (2021).
58. D. Moschella, D. Berretta, A. Tosi, *et al.*, "A 64 × 64 SPAD array for quantum ghost imaging with integrated TDCS and event-driven readout in a 40 nm CMOS technology," in *19th Conference on Ph.D. Research in Microelectronics and Electronics (PRIME)* (IEEE, 2024), pp. 1–4.
59. A. Orth, M. Ploschner, E. Wilson, *et al.*, "Optical fiber bundles: ultra-slim light field imaging probes," Sci. Adv. **5**, eaav1555 (2019).
60. R. Lussana, F. Villa, A. Dalla Mora, *et al.*, "Enhanced single-photon time-of-flight 3D ranging," Opt. Express **23**, 24962–24973 (2015).
61. C. Pitsch, D. Walter, L. Gasparini, *et al.*, "3D quantum ghost imaging," Appl. Opt. **62**, 6275–6281 (2023).
62. F. Nolet, V. Gauthier, S. Parent, *et al.*, "Quenching circuit discriminator architecture impact on a sub-10 ps FWHM single-photon timing resolution SPAD," Instruments **7**, 16 (2023).